

Disc galaxies with multiple triaxial structures *

II. JHK surface photometry and numerical simulations

D. Friedli@1, H. Wozniak@2, M. Rieke@3, L. Martinet@1 and P. Bratschi@1

@1 Observatoire de Genève, CH-1290 Sauverny, Switzerland @2 Observatoire de Marseille, F-13248 Marseille cedex 4, France @3 Steward Observatory, University of Arizona, Tucson AZ 85721, USA

Received 16 October 1995, accepted 2 February 1996

Abstract. We present detailed JHK surface photometry with ellipse fits of 13 galaxies selected from previous optical observations as likely candidates for having a secondary bar or a triaxial bulge within the primary bar. We have found 7 double-barred galaxies, 3 double-barred galaxies with an additional intermediate structure with twisted isophotes, and 3 galaxies with a bar and central twisted isophotes. A global analysis of the structural parameter characteristics in the I- and K-bands is presented. Various numerical models of galaxies with bars within bars are also analysed using the ellipse fitting technique and compared to the observations. A thorough review of the possible hypotheses able to explain this phenomenon is given with emphasis on the most likely ones.

Key words: Galaxies: photometry – Galaxies: structure – Galaxies: fundamental parameters – Galaxies: nuclei – Galaxies: evolution – Galaxies: barred

1. Introduction

In the first paper of this series (Wozniak et al. 1995, hereafter Paper I), we have presented a BVRI and H α survey of disc galaxies having multiple triaxial structures. More than one triaxial structure has been found in 22 galaxies, i.e. these galaxies show, inside the large-scale primary bar, at least one misaligned secondary bar or one structure with twisted isophotes.

Here, we present the detailed analysis of JHK surface photometry for a subsample of this survey. An extended and accurate knowledge of the structural parameters of observed single or multiple bars is a prerequisite to thorough comparisons with numerical simulations, and should give constraints and clues on the various processes

Send offprint requests to: D. Friedli, fri@scsun.unige.ch

* Based on observations collected at European Southern Observatory and Steward Observatory

of galactic secular evolution. Different kinds of information can be inferred from various bands, in particular the K-band traces fairly well the luminosity of the old stellar population (e.g. Rix & Rieke 1993; but see also Rhoads 1995) which thus opens the door to a better knowledge of the dynamical mass distribution (except dark matter). So far, published near-infrared surface photometry observations of large samples of galaxies have unfortunately not been very numerous (Baumgart & Peterson 1986; Terndrup et al. 1994; de Jong & van der Kruit 1994). Independently of the central problem of this paper, a significant increase of this type of data is certainly most desirable and necessary.

Since the paper of de Vaucouleurs (1974) more than twenty years ago, more and more compelling evidence has been accumulated that not only the majority of galaxies are barred (e.g. Sellwood & Wilkinson 1993), but also that some of them host at least two misaligned nested bars or one bar plus one triaxial bulge (e.g. Kormendy 1979, 1982ab; Jarvis et al. 1988; Friedli & Martinet 1993; Buta & Crocker 1993; Shaw et al. 1993, 1995; Paper I; Friedli 1996). These central isophotal deformations have thus been known for a long time and appear to be a widespread feature of disc galaxies although no reliable percentage can yet be given. The nuclear isophotes are subject to various asymmetries and twists resulting in a very complex morphology which indicates an intricate dynamics as well. However, the presence of dust confuses considerably the picture in optical bands. Since in the near-IR, especially in the K-band, the problems of dust absorption are greatly minimized (only about one-tenth of that at visible wavelengths), the existence and the shape of the various triaxial structures can be determined much more firmly.

The organization of the paper is the following: Sect. 2 is devoted to the description of our sample and reduction processes. In Sect. 3, we present an individual description of galaxies, the global properties of galaxies with multiple

triaxial structures, and a comparison with what was found with BVRI (Paper I). An analysis of various 3D numerical simulations with stars, gas and star formation is given in Sect. 4. A discussion is presented in Sect. 5 and our conclusions are summarized in Sect. 6.

2. The observations

Our sample is presented in Table 1. These galaxies represent a subsample of the ones analysed in Paper I. Observations were taken in both hemispheres and they are presented below in turn.

Table 1. Sample of observed galaxies

Names	PA _{disc}	<i>i</i>	References	Observations
(1)	(2)	(3)	(4)	(5)
NGC 470	149±3	51±4	a	E2.2
NGC 1097	134	46±5	b	E2.2
NGC 2681	50	32	f	S1.5
NGC 2950	110	50	f	S1.5
NGC 3081	123	33	f	S1.5
NGC 4314	121±10	30±5	c	S1.5
NGC 4340	85	47	f	S1.5
NGC 5850	157	37	f	S1.5
NGC 5905	45	40	d	S1.5
NGC 6782	40	26	f	E2.2
NGC 6951	135±10	28	e	S2.3
NGC 7098	50	66	f	E2.2
NGC 7479	37±2	44±2	a	S2.3

Columns (2) and (3): Published Position-Angle and inclination of the disc in degrees

Column (4): References for Columns (2) and (3): a = Garcia Gómez & Athanassoula (1991) / b = Ondrechen et al. (1989) / c = Wakamatsu & Nishida (1980) / d = van Moorsel (1982) / e = Boer & Schulz (1993) / f = our measurements

Column (5): E2.2 = observed at ESO 2.2m at La Silla / S1.5 = observed at Steward Observatory 1.5m at Mt. Bigelow / S2.3 = observed at Steward Observatory 2.3m at Kitt Peak

2.1. ESO sample

The observations were carried out during a run of two nights at ESO with the 2.2m telescope at La Silla. Photometric conditions were only realized during the first part of the first night and the second night. The photometry for NGC 1097 and NGC 6782 (especially the K-band) are thus not reliable. Over both nights and after complete reduction (co-added exposures), the FWHM seeing was between 1.1'' and 1.5''. On single exposure, it was between 0.9'' and 1.2''. The detector (IRAC2 camera) was a

256×256 NICMOS3 array. The pixel size is 0.49''; the field of view is thus about 2.1' large. Three galaxies (NGC 1097, NGC 6782, NGC 7098) extend beyond this field of view. The set of filters was chosen to be the standard JHK Johnson; we did not use the K' filter.

For each object, we took 2 series of 4 exposures on the object, galaxy or calibration star (science-frames), interspersed with sky exposures (sky-frames). The integration time was 150 seconds giving a total of 20 minutes per filter and per object. Each frame was bias subtracted and cleaned from cosmic rays as well as from cold and hot pixels. Flat-field exposures were obtained from exposures on a uniform illuminated blank screen. Flat-fields taken on the sky have been constructed for each filter by normalizing all sky-frames and averaging them using the median value of each coinciding pixels. These sky-flats were compared with the dome-flats; they show significant differences (cf. Moorwood et al. 1992). We achieve a better flat background with dome-flats than sky-flats. Then, each science-frame and sky-frame were divided by the flat-field. The sky background was removed using the mean of the two sky-frames taken just before and just after the science-frame, except for the first of the series for which there is only a sky exposure taken after it.

As the telescope is moved between the science and sky images, the exact position of the galaxy generally differs from one frame to another and some regions are not 8 times exposed. However, no correction was applied to these regions so that the effective field of view is less than 2.1' large. A scaling of the flux in such under-exposed region does not permit to achieve the same signal to noise ratio as the noise is also amplified. Thus, we prefer to restrict ourselves to the regions of good exposure.

Photometric calibrations were achieved by observing several AASO/ESO/ISO standard stars 3 times during the night. Our precision on the zero magnitude constant is 0.1 mag.('')⁻² except for NGC 1097 and NGC 6782.

2.2. Steward Observatory sample

The observations were carried out during two runs of one and four nights with the Steward Observatory 2.3m telescope on Kitt Peak and the 1.5m telescope on Mt. Bigelow. Photometric conditions were generally realized with a FWHM seeing of about 1.5'' at Kitt Peak and between 1.5'' and 1.7'' at Mt. Bigelow. Clouds were however present during the observations of the H-image of NGC 3081. The detector used was a 256×256 NICMOS3 array. At Kitt Peak, the pixel size was 0.6'' corresponding to a field of view of about 2.5' large, while at Mt. Bigelow the pixel size was 0.9'' and the field of view about 3.8'. Hereafter we will refer to the K-band although the filter used in both runs was in fact the K_s filter with a center wavelength of 2.16μm. Individual exposures were typically of 30 or 60 seconds with each galaxy being observed for a total of

40 minutes per filter at the 1.5m and 20 minutes per filter at the 2.3m.

The data were reduced by first subtracting dark-frames from the sky-frames. The skies were then median combined to create a sky-flat. The average of the surrounding sky-images were subtracted from each galaxy-frame which was then divided by the sky-flat. Images were registered and shifted to a common center before the final median combine. We encountered saturation problems with the H-band of NGC 2950 and K-band of NGC 4340. Indeed, the seeing was so good that more flux hit on the central pixels than usual. The array response is thus non-linear. Moreover, few of these pixels have a low sensitivity (bad pixels). This give a saturated-like shape at the surface brightness profiles.

Photometric calibrations were based on observations of Elias et al. (1982) standards. The photometric calibration is accurate to about 4% in flux based on the scatter of the data for individual standards. For the two galaxies observed under non-photometric conditions, our fluxes should not be trusted to any better than 30%.

2.3. Surface photometry analysis

We refer the reader to Paper I concerning the details of the technique of ellipse fitting, and the terminology we are using. The various effects which may affect the interpretation of the ellipticity e and the position-angle PA have also extensively been discussed in Paper I.

The following procedures have been performed to obtain the various colour maps. We have first aligned one image with respect to the other. The transformation was obtained by measuring positions of coinciding stars in the field of view. During the alignment, a scaling factor was introduced in order to get the same pixel scale in both bands. After the rebinning at the same scale, the differences of effective seeing between the images in different bands range from $0.05''$ to $0.1''$. This is similar to the centering accuracy when single exposure frames are co-added. We have however checked that this small difference does not introduce any artifacts. To do this, we have smoothed both images with a Gaussian filter to degrade the seeing to the same value. The resulting colour maps share the same features as the non-smoothed ones. Only the colour gradients are very slightly changed whereas the morphological features for bulges and bars are robust. As our signal-to-noise ratio is too low in any event in the discs to discuss their colours, we have chosen to display in Figs. 1 the non-smoothed colour maps.

Let us also briefly recall the main definitions. The *primary bar* is the bar with the larger spatial extent l_p whereas the *secondary bar* is the bar with the smaller spatial extent l_s . The angle between the two bars is θ . Positive values are for leading secondary bars whereas negative values are for trailing secondary bars (with regard to the primary bar rotation). The length ratio of the primary to

the secondary bar is $\beta \equiv l_p/l_s$. The integrated luminosity ratio between the two bars is $\gamma \equiv L_p/L_s$ where L_p and L_s are the luminosity of the primary and secondary bar. Note that L_p is defined as the luminosity inside the isophote of semi-major axis length l_p so that it includes the luminosity of the secondary bar, the bulge and the nucleus. The same definition holds for L_s . The maximum ellipticities of the secondary and primary bar are e_s^{\max} and e_p^{\max} . In cases where more than two triaxial structures are present, they are simply numbered from 1 to n starting from the largest to the shortest component. So, the semi-major axis length ratio of the component i to the component j is β_{ij} whereas the integrated luminosity ratio is γ_{ij} .

3. Results

3.1. Individual description of galaxies

We give below a description of the main features observed for each galaxy. In general, the various parameters mentioned are always measured on the K-image because this band is the one least affected by dust extinction amongst JHK, and it best traces the old population and hence mass. At the end of the paper, Figs. 1 show for each galaxy in our sample the surface brightness μ , ellipticity and PA profiles for JHK-filters, the greyscale and contour maps in J- and K-bands as well as the greyscale map of the J-K colour. For a few galaxies other bands or J-H or H-K colour maps are displayed.

NGC 470. In Paper I we have detected two triaxial structures in this galaxy usually classified SA(rs)b. However, this was one of the most difficult case to analyse since this galaxy contains a lot of dust. Although we confirm here the presence of one primary bar, the secondary component could be a bulge with the same orientation angle as the disc. The deprojection is now much more difficult as the disc appears warped (NGC 470 is in weak interaction with NGC 474). It is thus questionable to assume that the outermost isophotes of the disc are circular. The most sensible interpretation is that of a triaxial bulge as the PA profiles do not show any plateau but are twisted in the innermost regions. This central structure is clearly visible in the J-K colour map as a very red component ($1.3 \lesssim J - K \lesssim 1.6$).

NGC 1097. Our BVRI profiles obtained in Paper I were similar to those obtained in the K-band by Shaw et al. (1993) and clearly indicated the presence of two bars separated by a ring. However, the present data in JHK-bands give a completely new view of the nuclear region. Indeed, the circumnuclear ring is not closed. Like Quillen et al. (1995), we have found a small secondary bar ended by a trailing spiral-like structure which seems to be an extension of the dust lanes. The isophote twists just outside the end of the secondary bar are due to this spiral-like structure. The resolution of Shaw et al. (1993) ($1.24''/\text{pixel}$)

did not allow them to clearly detect this peculiar structure although the isophote shape of their Fig. 1a suggests some spiral structure at the secondary bar end. Knapen et al. (1995) have found a similar feature in NGC 4321 but in that case additional leading spiral arms are also present. Dust prevents the detection of the secondary bar on HST V-images (Barth et al. 1995).

The nature of the spiral-like structure is yet unclear. Is it a ring crossed by two dust lanes in such a way that it appears not closed or does the star formation occur on an actual spiral density wave (giving rise to a “hotspot” look to the ring in the K-band)? The western dust lane, interpreted by Quillen et al. (1995) to be on the near side of the galaxy, appears on the colour map but is more difficult to see on the K-image. Moreover, the spiral-like pattern has also been observed in mid-infrared (Telesco et al. 1993) and radio observations (Hummel et al. 1987). However, as the dust is also visible on the K-band in the region of the primary bar, we cannot exclude that, even at $2.2\mu\text{m}$, isophotes could be distorted by the darkening. Note that due to poor weather conditions during the observations, we are not able to display any colour maps in Fig. 1.

NGC 2681. It is difficult to identify unambiguously a secondary bar in this galaxy, and the abundant dust seen in our BVRI-images could be responsible for the apparent nuclear structure. Indeed, in the K-band, the innermost ellipticity maximum is strongly decreased although still present. The primary bar shows a significant isophote twisting (15° – 20° depending on the band). The J–K colour map shows a blue Seyfert nucleus (as in Paper I) whose J–K is roughly 0.5 mag. bluer than the surrounding region. As the size of this nucleus is closed to the seeing value, we have displayed the colour map obtained from convolved images with approximately $3''$.

NGC 2950. The $0.9''$ resolution of our images prevents an accurate determination of the structural parameters of the secondary bar. The signature of this small bar appears less pronounced in K-band than in I-band. The profiles are thus more noisy. Moreover, the image taken in the H-band is saturated. However, in the region of the expected secondary bar, the PA really shows a plateau, especially pronounced in the J-band. The J–K colour map shows an unusual structure. The red emission is indeed aligned with the primary bar although its distribution is asymmetric. There is no red emission towards the south part of the primary bar.

NGC 3081. In the K-band, the secondary bar observed in optical bands by Buta (1990) as well as in Paper I is clearly confirmed. It is also very luminous with respect to the primary bar. Indeed, it creates a very significant bump in the surface brightness profile. The nuclear ring does not appear in the K-band, suggesting that it is not luminous enough and it is better traced by dust and/or star forma-

tion than by old stars. The secondary bar also appears in the J–K colour map as a very red and elongated structure ($\text{J–K} \approx 1.0$). Note that the H-image is not photometric.

NGC 4314. Using the HST telescope, Benedict et al. (1993) have found an oval distortion of $4''$ (semi-major axis length) in the nuclear region. However, with our JHK data at $0.9''$ resolution it is impossible to confirm the presence of such an oval. We find a more or less boxy shape of the inner isophotes due to the spots of star formation along the nuclear ring. We cannot resolve these spots because of the blurring by seeing. The major-axis of these boxy isophotes is aligned with the primary bar. This creates the small innermost maximum on the ellipticity profiles at $4.8''$ with roughly the same PA as the primary bar ($\theta = -12^\circ$). This innermost ellipticity maximum depends on the wavelength and could therefore be biased by dust absorption. We have nevertheless decided to associate the innermost structure with the secondary bar of Benedict et al. (1993) because of their $0.13''$ resolution, although it is not clear why this object shows the largest values of β and γ (cf. Table 2). Moreover, on HST images $\theta = -3^\circ$. The nuclear ring is clearly visible in the J–K colour map ($0.25 \lesssim \text{J–K} \lesssim 0.40$). Shaw et al. (1995) claimed that the nucleus of this object is blue inside $2''$. Due to our point spread function we are unable to confirm their result. The red nucleus visible in our J–K colour map could be an artifact: all stars in the field show similar features.

NGC 4340. The innermost structure regarded as a secondary bar in Paper I seems to be also present in JHK-images (K-band is saturated). It is roughly aligned in projection with the primary bar ($\theta_{13} \approx -3^\circ$). The J–H colour map displays a blue central region ($\text{J–H} \approx -0.1$) as compared with the rest of the primary bar ($\text{J–H} \approx 0.1$).

NGC 5850. Without any surprise, the JHK-images confirm the double-barred nature of this galaxy. In particular, the secondary bar appears in the J–K colour map as a redder structure as well. It is also surrounded by a very faint red ring which is difficult to see on the greyscale figure.

NGC 5905. The secondary bar of NGC 5905 is confirmed on H- and K-images with the same value for the maximum ellipticity (no J-image). At the end of the secondary bar a very red circumnuclear ring appears in the H–K colour map. This ring is correlated with the H α and the blue B–I ring observed in Paper I. However, the reddest part of the H–K ring ($\text{H–K} \approx 0.8$) does not coincide with the bluest regions of the B–I ring ($\text{B–I} \approx 1.8$) contrary to most galaxies with nuclear rings. NGC 5905 is one of our two cases with such phenomenon (cf. NGC 6951).

NGC 6782. This object clearly is a double-barred galaxy. Indeed we detect the secondary bar surrounded by a stellar ring in all three bands. The dust distribution seen in

Table 2. Projected structural parameters of the various components for the K-band

Names	Type	1st component			2nd component			3rd component			Ratios				Central		
		l_1	ϵ_1^{\max}	PA ₁	l_2	ϵ_2^{\max}	PA ₂	l_3	ϵ_3^{\max}	PA ₃	β_{12}	θ_{12}	γ_{12}	β_{13}	θ_{13}	γ_{13}	
		(1)	(2)	(3)	(4)	(5)	(3)	(4)	(5)	(3)	(4)	(5)	(6)	(7)	(8)	(6)	(7)
NGC 1097	B+B	$I \approx 80$	$I 0.67$	$I 147$	10.3	0.46	30				7.8	-63	$I 3.8$				no colour
NGC 2681	B+B	28.7	0.34	80	4.9	0.11	5				5.8	+75	1.8				o
NGC 3081	B+B	40.9	0.65	65	10.3	0.37	113				4.0	+48	2.3				rs
NGC 4314	B+B	≈ 75	0.69	143	5.6	0.19	131				13.4	-12	7.5				r
NGC 5850	B+B	83.7	0.68	112	9.2	0.31	46				9.1	-66	3.5				r,rs
NGC 5905	B+B	36.6	0.61	20	5.7	0.19	133				6.5	+67	3.8				$H-K$
NGC 6782	B+B	35.8	0.54	178	5.2	0.40	149				6.8	-29	3.0				$J-H$
NGC 470	B+T	31.6	0.55	14	7.6	0.46	150				4.1	-46	2.9				rs
NGC 6951	B+T	56.7	0.59	85													r,o
NGC 7479	B+T	45.6	0.80	6													o
NGC 2950	B+T+B	37.6	0.45	152				6.2	0.25	92				6.1	+60	2.4	-
NGC 4340	B+T+B	$J 51.7$	$J 0.41$	$J 32$				$J 5.0$	$J 0.10$	$J 35$				$J 10.3$	$J -3$	$J 4.9$	$J-H$
NGC 7098	B+T+B	57.3	0.57	50				14.4	0.32	71				3.9	-21	2.2	-bc

Column (2): Suggested classification. B = barred structure / T = twisted structure

Column (3): Projected semi-major axis of the component i in arcsec defined at the minimum of ellipticity. Values coming from other bands are preceded by the corresponding letter

Column (4): Projected maximum ellipticity of the component i

Column (5): Projected position-angle of the component i in degree at its maximum of ellipticity

Column (6): Projected semi-major axis length ratio of the component i to the component j

Column (7): Projected relative angle between the component i and the component j . A positive angle means the structure j is “leading” the structure i while a negative angle mean it is “trailing”. Values in italic indicate that the sense of rotation is unknown and the trigonometric convention is used

Column (8): Integrated luminosity ratio of the component i to the component j

Column (9): bc = blue center / o = other features / r = red ring / rs = red secondary bar

B-I colour map (Paper I) is thus better explained by taking into account this bar+ring structure. Between the two bars, the ring creates a bump in the PA profiles. It does not have the same projected orientation as the secondary bar. The squares appearing on the images result from the bad removal of bright foreground stars on sky-frames. The plateau in the outermost part of the surface brightness profile in the K-band is due to a change of the weather conditions. The sky brightness is thus poorly subtracted. We have computed the J-H colour map instead of the J-K one. The nuclear ring ($J-H \approx 0.5$) is clearly visible as a redder structure than the primary bar ($J-H \approx 0.3$).

NGC 6951. We cannot unambiguously confirm the secondary bar suggested in Paper I due to the strong isophote twists. This twisted structure is surrounded by a red ($J-K \approx 1.35$) nuclear ring visible on J-K colour map while the surrounding region has $J-K \approx 1.0$. The morphology of this ring is roughly the same on H α , B-I and J-K maps. Moreover, the VLA radio maps of Saikia et al. (1994) show a spiral-like structure in the gas component which is compatible with the presence of a bar. However, the biggest J-K spot located N (on the original J-K map but badly

reproduced on the greyscale figure) is not exactly coincident with the corresponding one in the B-I map (cf. NGC 5905). Also, the reddest part of the J-K ring is in the SW, where the dust darkening is the greatest. The various hotspots are in fact spectacularly resolved into numerous smaller star forming regions with HST V-image (Barth et al. 1995). Their image does not show any secondary bar. It is thus not clear if the observed twists could result from the few intense sites of star formation along the nuclear ring and/or the dust pattern inside the ring.

NGC 7098. The B+T+B classification of Paper I is confirmed. Both maxima in ellipticity are well separated by a triaxial bulge. This bulge shows a twist of almost 25° . The J-K colour map does not display any peculiar structure.

NGC 7479. It is not possible to detect reliably any structure apart from the main bar. This galaxy is already too inclined (see Sect. 4.2) and the equatorial dust obscures the region where the secondary bar detection could be possible. A careful inspection of the J-K colour map indicates that the whole galaxy is crossed by a dust lane. However,

the spatial distribution seems not to be symmetric and the central part shows a clear isophote twists.

3.2. Global properties

The various projected structural parameters in the K-band for the galaxies discussed in Sect. 3.1 are summarized in Table 2 and displayed in Figs. 2, 3 and 4.

For the category B+B including NGC 470, $4.0 \leq \beta \leq 13.4$ and $1.8 \leq \gamma \leq 7.5$, and a typical double-barred galaxy has $\beta \approx 7.2$, $\gamma \approx 3.5$, $e_s^{\max} \approx 0.31$, and $e_p^{\max} \approx 0.58$. For the category B+T+B, $3.9 \leq \beta_{13} \leq 10.3$ and $2.2 \leq \gamma_{13} \leq 4.9$, and mean values $\beta_{13} \approx 6.8$, $\gamma_{13} \approx 3.2$, $e_3^{\max} \approx 0.22$, and $e_1^{\max} \approx 0.48$. As already observed for the I-band (Paper I), generally $e_s^{\max} < e_p^{\max}$. This may be an observational effect due to seeing and pixel size which affect most central structures. But, on the other hand galactic centers are dynamically hot and the formation of weaker bars are not unexpected in that case (see e.g. Athanassoula 1983).

In their sample, Shaw et al. (1995) have found a majority of galaxies with blue nuclear regions in the near-IR colours J-H and H-K. On the contrary, this feature is not dominant in the sample presented here since only 1 galaxy (NGC 4340) in 13 has a blue centre in J-K. NGC 4340 has also a blue centre in J-H. Thus, its colour does not result from the central saturation of the K-image. Moreover, the blue region is larger than the saturated one. Another galaxy (NGC 2681) has a blue centre of a few pixels but this is surely due to the Seyfert nucleus (cf. Paper I). On the contrary, a red secondary bar is clearly observed in 3 galaxies, and a red nuclear ring in 5 galaxies.

Due to the poor and biased statistics, no reliable percentage of double-barred galaxies among barred galaxies can be given. In recent years the number of such galaxies has strongly increased due to the advent of optical CCD's and infrared arrays. This certainly indicates that this feature might be more common than previously estimated. Figure 5 shows the dependence of the projected structural parameters with respect to Hubble type T of the galaxies both in the I- and K-bands. In our sample, no double-barred galaxies have been found with types later than T=3. No preferential angle θ has been found and there is no correlation between the Hubble type and θ . In particular, leading secondary bars are not preferably found in late-type spirals. In the I-band sample of 13 double-barred galaxies, 6 were leading and 7 trailing. The above results do not change after deprojection (see Sect. 3.4). With a few exceptions and a relatively high scatter, early-type galaxies seem to have lower β and γ than late-type galaxies. The best correlation is observed for γ in the K-band but the number of galaxies is still small. This can easily be explained by the fact that the Hubble sequence is also a sequence of bulge to disc luminosity (or mass) ratio (increasing bulge to disc luminosity with decreasing T). The maximum ellipticity of the secondary bars does not

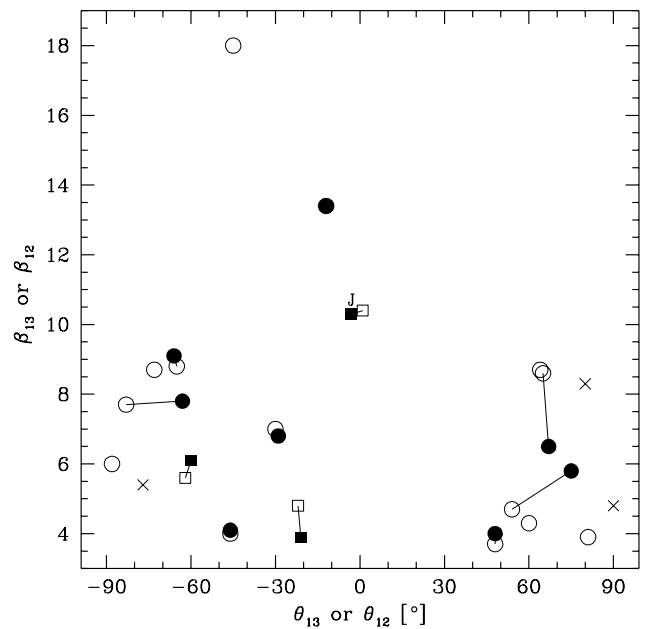


Fig. 2. Relation in the K-band between θ_{12} and β_{12} (full circles) and θ_{13} and β_{13} (full squares). The open circles and squares correspond to the values found in the I-band (Paper I). The solid lines link identical galaxies. The crosses correspond to various numerical simulations. The J letter indicates a measurement in the J-band

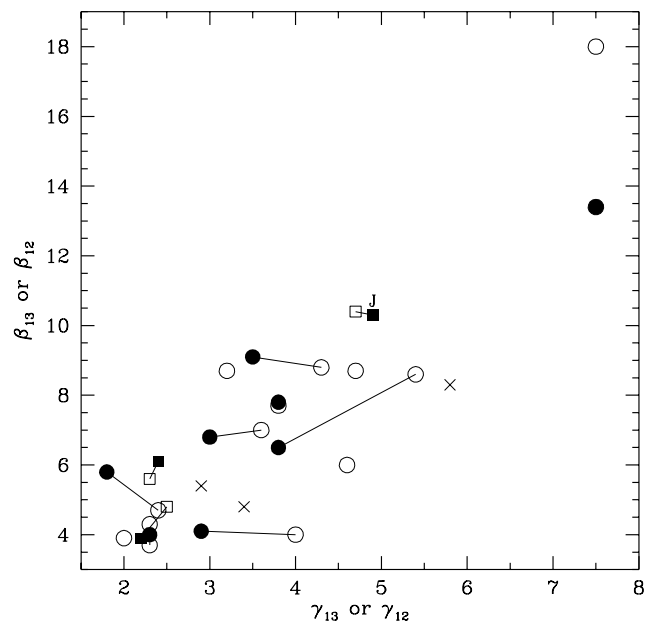


Fig. 3. The same as Fig. 2 but for the relation between γ_{12} and β_{12} (full circles) and γ_{13} and β_{13} (full squares)

seem to correlate with the Hubble type whereas late-type galaxies could have higher maximum ellipticity.

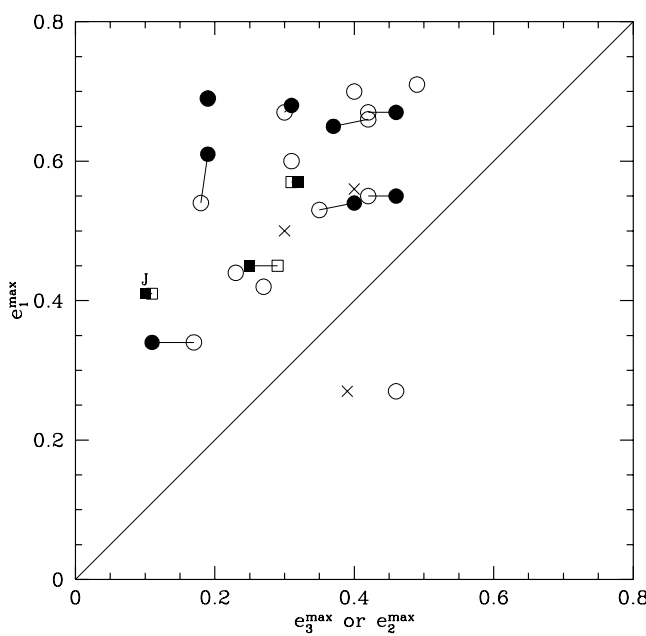


Fig. 4. The same as Fig. 2 but for the relation between e_1^{\max} and e_2^{\max} (full circles) and e_1^{\max} and e_3^{\max} (full squares)

3.3. Comparisons with BVRI

Although the values of the structural parameters θ and β are noticeably the same between Paper I (I-band) and the present paper (K-band), a few pronounced discrepancies deserve an explanation. Indeed, for NGC 1097 we find a difference of 20° for θ , while β increases from 7.7 to 7.8. This could be explained by the presence of dust which leads to an erroneous determination in the I-band as the darkening alters the morphology of the isophotes. For NGC 5905, the same explanation holds but the dust essentially modifies the β ratio (6.5 instead of 8.6 in I-band), as θ agrees between I- and K-bands within 5° . Note that in both cases, the primary and the secondary bars are longer in K-band than in I-band. Again, dust darkening could explain the differences both in β and θ for NGC 2681 (for θ , 75° instead of 54° in I-band; for β , 5.8 instead of 4.7 in I-band). The dust distribution does not follow regular lanes as in most other barred galaxies but is rather distributed on fine threads over the whole disc. The dust is also visible in the K-band.

The observed intervals of β and γ are very similar in I- or K-bands with a distinct upper limit given only by one galaxy, i.e. NGC 5728 (I-band) and NGC 4314 (K-band). These galaxies are either very peculiar, or there is an observational bias toward the lowest, easiest to detect, β values. Globally, a typical (mean) double-barred galaxy has similar values for its structural parameters in I- or K-bands. However, in the subsample measured in I- and K-bands, the majority of γ are smaller in the K-band than in the I-band (see Fig. 3) with respective mean values of

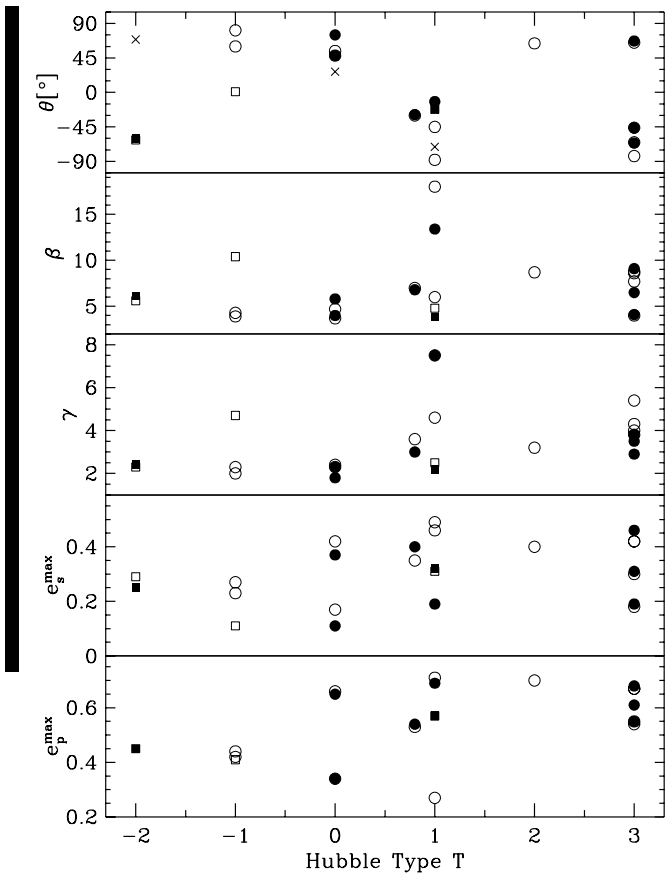


Fig. 5. Projected values of θ , β , γ , e_s^{\max} , and e_p^{\max} as a function of the Hubble type T. The full circles are for the K-band whereas the open circles correspond to the I-band (Paper I). The crosses come from Buta & Crocker (1993)

2.9 and 3.5. Since, the K-band is a better tracer of the stellar mass distribution, one is led to conclude that the central mass concentration is slightly underestimated in the I-band. Linear fits show that the slope of the relation between γ and β is similar for both bands.

The mean values for secondary and primary bar ellipticities are about 10% lower in K-band than in I-band. As far as we are concerned with the ellipticity of the secondary bar, the differences between I- and K-bands could arise from the different seeing conditions and resolutions (that give different seeing samplings). For ESO images, taken at $0.49''$ resolution and a seeing of roughly $1''$, all four galaxies have a greater maximum ellipticity for the secondary bar in the K-band. This is not the case for the images taken at $0.6''$ and $0.9''$ of resolution with $1.5''$ – $1.7''$ of seeing which show a decrease of e_s^{\max} .

Finally, it should be noted that for the category B+B primary bar lengths measured in the K-band are greater than the ones in the I-band. The amplitude of this effect is in no case greater than about 13%. This result has been carefully checked since we have scaled the K-band pixel

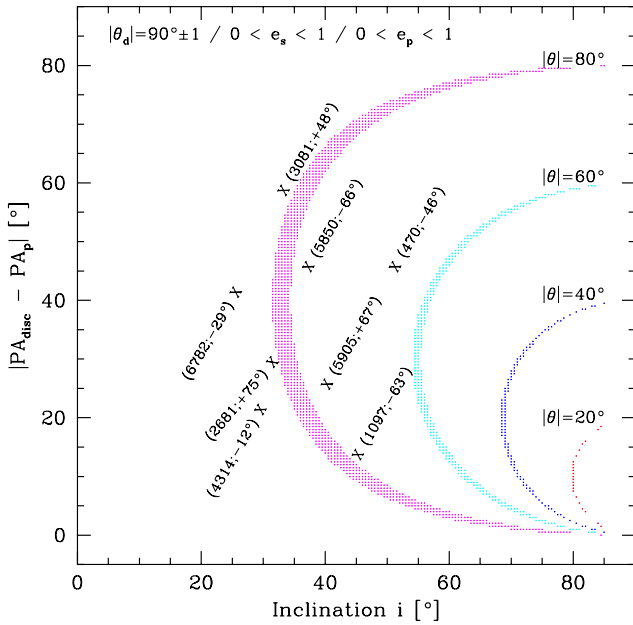


Fig. 6. The regions where the deprojected angle between the two bars $|\theta_d|=90^\circ$ are displayed in the diagram $|\text{PA}_{\text{disc}} - \text{PA}_p|$ versus i for various observed angle θ and any ellipticities. Real galaxies are plotted with a cross and a label (NGC number; θ). No one is close to these regions

size (expressed in $('') \cdot \text{px}^{-1}$) with respect to the value in the I-band. Assuming that the I-band pixel sizes (one for each telescope used) are free of errors, we have measured positions of at least 3 stars visible in both I- and K-images. The geometric transformation from I-band coordinates to K-band ones give us the true pixel size. We systematically found significant differences with the theoretical value or the value given by observer's manuals. The lengths given in Table 2 use the true pixel size.

3.4. Deprojections

How to deproject images is a long-standing problem we do not want to develop here (see e.g. Binney & Gerhard 1995, and references therein). However, it is necessary to check that the deprojected angles between the two bars θ_d really do not take any peculiar value, in particular 90° . Deprojections are performed as in Paper I. Figure 6 displays, in the diagram $|\text{PA}_{\text{disc}} - \text{PA}_p|$ versus the inclination angle i , the regions where the deprojected angles between the two bars $|\theta_d|=90^\circ$ for various observed angle θ and any ellipticities. Some of the observed galaxies are also plotted and one can see that none is close to these regions. The two bars are really misaligned. After deprojection, there is still roughly half leading and half trailing secondary bars. This is a crucial point for the understanding of the bar-within-bar phenomenon (see Sect. 5).

4 Numerical simulations

Thanks to numerical simulations including stars and gas, Friedli & Martinet (1992, 1993; Combes 1994) have shown that the secondary stellar bar can be created from a decoupling of the central dynamics triggered by gas flood accreted towards the centre by the primary stellar bar. The two bars have then two different pattern speeds with the secondary bar being the faster.

We have computed a new set of simulations which mainly differs from the one by Friedli & Martinet (1993) in the following way: 1) Model B_{no} . The particle number is doubled, i.e. $N_g = 20\,000$, $N_* = 200\,000$, and the mass of the various components has been decreased, i.e. $M_g = 0.055$ (instead of 0.1), $M_b = 0.05$ (0.1), $M_d = 0.50$ (0.8). 2) Model B_{sf} . The same as model B_{no} but star formation is included (see Friedli & Benz 1995 for details). We analyse below in the same way as the observations (i.e. with the ellipse fitting technique) various 2D density projections of the 3D numerical simulations. Only star particles have been used unless otherwise stated. As for the observations, the 2D grid used is 256×256 . Of particular interest are the time evolution and orientation changes of the structural parameters. The typical evolution of the stellar isodensity contours can be found in Fig. [4] of Friedli & Martinet (1993).

4.1. Generic model

The time evolution of the structural parameters of our generic model B_{no} is presented in Fig. 7. The time dependence of θ is clearly seen and indicates the presence of two different pattern speeds. At first order, these numerical models fairly well reproduce the observed features of double-barred galaxies (two distinct PA's, maximum ellipticities, and surface brightness slopes). The values of $\beta \approx 4.8$, $\gamma \approx 3.4$, $e_s^{\text{max}} \approx 0.40$ and $e_p^{\text{max}} \approx 0.56$ are also very similar to what is observed (see Figs. 2, 3, 4).

Let us concentrate on two peculiar angles: 1) $\theta \approx 90^\circ$. This particular orientation leads to the best determination of the end of the secondary bar by looking at the position of the distinct minimum ellipticity (close to zero). The transition from PA_s to PA_p is also very sharp. 2) $\theta \approx 0^\circ$. By definition, there is no transition from PA_s to PA_p . The ellipticity dip between the two maxima is strongly reduced. Thus, it could be very difficult to highlight galaxies with nearly parallel bars within bars, even in the face-on ones, with morphological criteria only.

Contrary to the end of the secondary bar, the end of the primary bar is generally difficult to infer from ellipse fits mainly because of the significant amplitude of the spiral arms (the ellipticity does not go to zero and the PA is progressively twisted). So, we chose to associate the primary bar end with its corotation radius. Another problem is that near the primary bar end both the grid resolution and the particle density are becoming poor. It is then

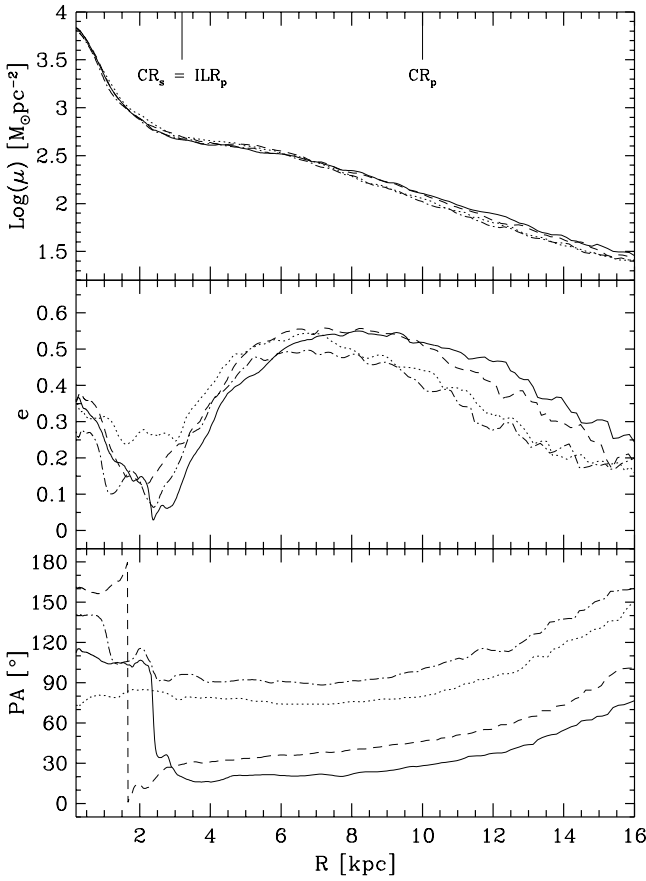


Fig. 7. Plots of stellar surface density μ , ellipticity e and position-angle PA profiles as a function of the semi-major axis of the fitted ellipse, at various times $t = 1270$ Myr (solid curve; $\theta \approx 90^\circ$), $t = 1225$ Myr (dotted curve; $\theta \approx 0^\circ$), $t = 1255$ Myr (dashed curve; $\theta \approx 60^\circ$), and $t = 1210$ Myr (dot-dashed curve; $\theta \approx -50^\circ$). Model B_{no} seen face-on

necessary to smooth slightly the surface density which can alter the values of the structural parameters, in particular the secondary bar ellipticity (cf. Fig. 8). This smoothing effect is similar to the one induced by seeing or pixel size in real observations.

Between the two bars, a massive non-circular broad gaseous ring is present (see Fig. [3] of Friedli 1996). It is located inside the CR_s and is in fact essentially controlled by the secondary bar, i.e. it has the same pattern speed and orientation. Its contribution to the total surface density is not negligible as can be seen on Fig. 8 where ring signatures are clearly visible: A new maximum appears in the ellipticity profile ($e_{\text{ring}}^{\text{max}} \approx 0.35$) as well as significant twists in the PA profile. Some gas-induced distortions in the stellar isophotes are also observed.

4.2. Projection effects

One of the big advantages of 3D numerical models is the possibility to perform 2D projections in whatever direc-

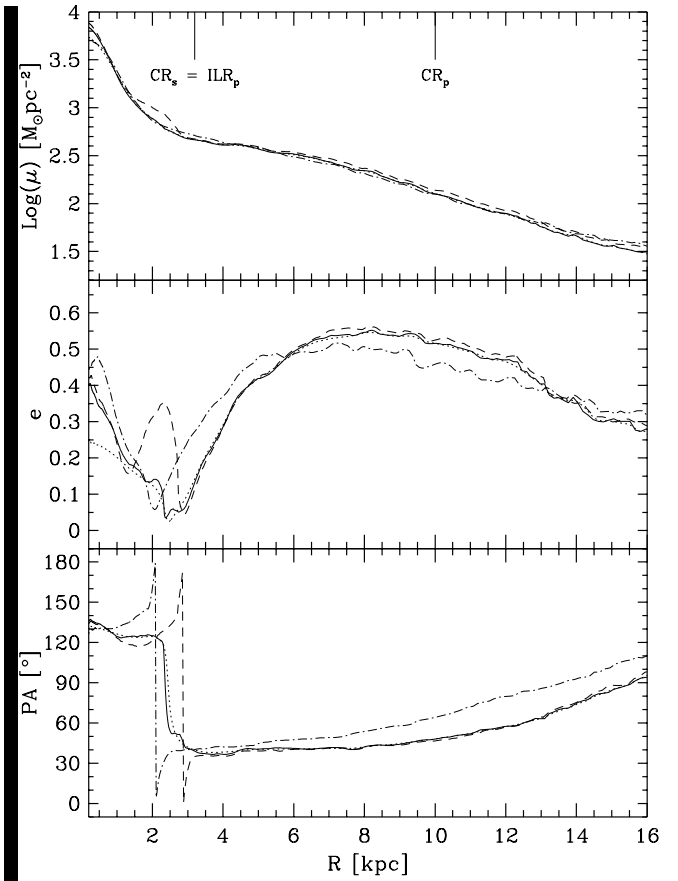


Fig. 8. Comparison of μ , e and PA profiles as a function of the semi-major axis of the fitted ellipse between the model B_{no} ($t = 1270$ Myr) with low smoothing (solid curve), with high smoothing (dotted curve), with gas mass included (dashed curve), and the model B_{sf} ($t = 1390$ Myr; dot-dashed curve). Galaxies are seen face-on

tion. Figure 9 shows the changes that are induced in the structural parameters by the progressive increase of the galaxy inclination i for the model B_{no} at $t = 1270$ Myr and with $|\text{PA}_{\text{disc}} - \text{PA}_p| \approx 45^\circ$. When i increases, the PA of the secondary bar becomes more and more twisted, e_s^{max} decreases and the ellipticity is no longer close to zero between the two bars (the ellipticity dip nearly vanishes). These twists clearly indicate that the secondary bar is a 3D triaxial structure, and not simply a 2D thin bar. The most striking effect is the disappearance of distinct double-bar characteristics as soon as $i \gtrsim 45^\circ$, although $\theta \approx 90^\circ$ in this case which is a very favourable situation. It is thus very difficult to highlight bars within bars in such galaxies at least with morphological criteria only. Moreover, the maximum inclination allowed for an easy detection of double-barred galaxies depends both on θ and e_s^{max} whose values should not be too small.

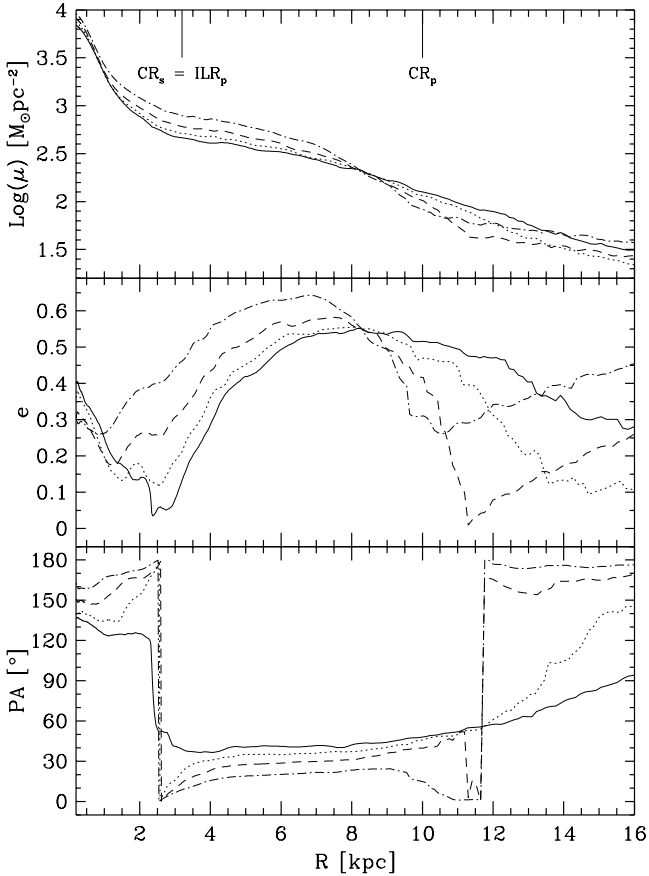


Fig. 9. The same as Fig. 7 but at various inclinations $i = 0^\circ$ (solid curve), $i = 30^\circ$ (dotted curve), $i = 45^\circ$ (dashed curve), and $i = 60^\circ$ (dot-dashed curve). Model B_{no} at $t = 1270$ Myr

4.3. Role of star formation

The main differences between the generic model B_{no} (at $t = 1270$ Myr) and the one with star formation B_{sf} (at $t = 1390$ Myr) can be seen on Fig. 8. The time evolution of the two models being slightly different, the comparison cannot be synchronized. Star formation mainly occurs along spiral arms outside the primary bar corotation as well as along the secondary bar major axis as well as along the nuclear ring inside the secondary bar corotation. As a consequence, these numerous new stars induce a significant increase of e_s^{max} . These new stars are dynamically cold and form a much thinner bar than the one made of the initial, dynamically hot, old stars. The secondary bar is also shorter whereas e_p^{max} is slightly decreased. Another change concerns the significant decrease of the gas influence onto stellar isophotes since about half of its mass has been turned into stars inside the CR_s .

5. Discussion

The general problem of misaligned, aligned, or twisted structures within primary stellar bars have been partially reviewed both observationally and theoretically (Friedli & Martinet 1993; Friedli 1996; and references therein). In this discussion, the various possibilities are synthesized in view of the results of this paper.

5.1. Misaligned secondary bars

Many explanations can be put forward in order to explain the phenomenon of secondary misaligned stellar bars (i.e. $\theta_d \neq 0^\circ$) within primary stellar bars.

- 1) The observed misalignment is due to projection effects:
 - There are only one primary bar and a round centre which simply appeared barred in projection. In the majority of cases, this possibility does not hold since the position angle of the secondary structure clearly differs from that of the disc.
 - The two bars are simply perpendicular (i.e. $\theta_d = 90^\circ$) such that the primary bar is made of orbits trapped by the x_1 family, and the secondary bar is built with orbits trapped by the x_2 family. This can be true in some specific cases (e.g. NGC 1317) but numerous examples of nearly face-on galaxies with small θ (e.g. NGC 1291, NGC 6782; see also Fig. 6) rule out this possibility as a universal explanation. In general, $\theta_d \neq 90^\circ$.
- 2) This peculiar morphology is an observed artifact due to specific central patterns of star formation or dust absorption. This argument is generally to be excluded since, in the majority of cases, this phenomenon is observed in the near-IR as well.
- 3) A permanent misalignment of two purely stellar bars with the same pattern speed is very unlikely due to the very short lifetime expected. Strong gravitational torques will indeed quickly align the two bars.
- 4) Shaw et al. (1993; see also Combes 1994) have suggested that the gravitational potential generated by large amounts of leading (with regard to the primary bar) gas around the ILR of the galaxy could be responsible of the presence of secondary or twisted stellar structures. However, trailing secondary bars cannot be explained this way. Moreover, bars within bars are also observed in SB0 galaxies whose gas mass fraction is generally very low.
- 5) The best way to reconcile theory and observations consists in postulating that the secondary stellar bar rotates faster than the primary stellar bar as suggested by Pfenniger & Norman (1990). Friedli & Martinet (1993) have demonstrated the viability of such systems which form through a dynamical decoupling between the central and outer parts of the galaxy. This decoupling is essentially made possible by the primary bar-driven gas fueling. Tagger et al. (1987) have invoked nonlinear mode coupling to explain multiple pattern speeds of bar and spiral arms.

6) In order to explain the fueling of AGN's, Shlosman et al. (1989) have invoked the formation of a small-scale gaseous bar within a large-scale primary bar. Simulations by Heller & Shlosman (1994) have shown that this process is transient since fragmentation and dynamical friction quickly dissolve the gaseous bar. So, if this process is to be very effective in powering AGN's, it is not obvious how to link it to the existence of persistent misaligned secondary stellar bars.

5.2. Aligned secondary bars

Two explanations can be given in order to explain secondary aligned stellar bars (i.e. $\theta_d = 0^\circ$) within primary stellar bars. This is observed in NGC 1326 after deprojection (Paper I) as well as in NGC 4314 (Benedict et al. 1993) and in NGC 4321 (Knapen et al. 1995).

- 1) There is a single pattern speed associated with a single bar with two ILR's. The secondary bar is made of orbits trapped by the x_1 periodic orbit family inside the inner ILR whereas the primary bar is supported by the x_1 outside the outer ILR to close to the CR. Between the two ILR's, the x_2 dominates, gaseous orbit crossings are present and spot- or ring-like structures are likely to be formed there.
- 2) There are two different pattern speeds associated with the two bars (see point 5) in Sect. 5.1) and the system is observed in that peculiar configuration.

5.3. Twisted isophotes

In order to explain twisted stellar isophotes (i.e. $\theta_d = \theta_d(R)$) within primary stellar bars, the following explanations can be put forward.

- 1) The observed twists come from projection effects:
 - On a triaxial bulge. This is the most likely explanation for early-type galaxies (e.g. NGC 2950). Note that a triaxial bulge or a secondary (thick) bar could in fact be physically indistinguishable.
 - On a thin bar with strongly varying ellipticity with radius. This can explain many of the weak PA variations ($\lesssim 10^\circ$) observed along some primary bars (e.g. NGC 5850).
- 2) The twists are due to specific central patterns of star formation or dust absorption. In particular, intense and irregular rings of star formation can produce isophote twists even in the K-band (e.g. NGC 6951). Similarly, the absorption in the near-IR can remain high in some very dusty galaxies (e.g. NGC 1097). However, in general this explanation can be dismissed when such twists are observed in the near-IR as well.
- 3) The twists are generated by spiral arms. This generally occurs at the end of the primary bar but can also be observed at the end of the secondary bar (e.g. NGC 1097).
- 4) The twists are generated by large amounts of gas (see point 4) in Sect. 5.2). This could certainly be an adequate

explanation for some gas-rich late-type galaxies with leading isophote twists.

6. Conclusions

The main results of this paper can summarized as follows:

- 1) In our sample, near-IR images clearly confirm the existence of galaxies with multiple triaxial structures, and in particular double-barred galaxies. In the most dust-rich galaxies some central triaxial signatures, like isophote twists, could however still be absorption artifacts.
- 2) The K-band values of the structural parameters are thought to trace better the real morphology of the bulk of the stellar mass. With some marked exceptions, the structural parameters in the K-band are similar to the ones in the I-band. In particular in double-barred galaxies, the primary bar lengths measured in the K-band are systematically greater (at most 13%) than the ones in the I-band.
- 3) The various triaxial structures are robust to standard deprojection. The deprojected angle θ_d between the two bars does not take any preferential value (like 0° or 90°). There are roughly half leading and half trailing secondary bars.
- 4) Numerical models of two nested bars with two different pattern speeds fairly well reproduce to first order the observed features of double-barred galaxies (two distinct PA's, maximum ellipticities, and surface brightness slopes). The analysis of various 2D projections of 3D numerical simulations indicates that these bar-within-bar features are generally strongly reduced as soon as $i \gtrsim 45^\circ$. Similarly, small θ and/or e_s^{\max} are not favourable for bringing double-barred galaxies to the fore.
- 5) For the K-band, double-barred systems (8 galaxies including NGC 470) have (projected values):
 - Primary to secondary bar length ratios ranging from 4.0 to 13.4 with a mean value of 7.2.
 - Primary to secondary bar luminosity ratios ranging from 1.8 to 7.5 with a mean value of 3.5.
 - The mean maximum ellipticity is 0.58 for the primary bar.
 - The mean maximum ellipticity is 0.31 for the secondary bar.
- 6) Our poor and biased sample does not allow us to infer any firm percentage or dependence with Hubble type of the galaxies with bars within bars. The following can nevertheless be said: – In our sample, no double-barred galaxies with types later than T=3 have been found. So, galaxies with bars within bars are certainly less abundant in later than earlier types. – In the K-band, the luminosity ratio γ increases from earlier to later types.

Clearly, misaligned secondary bars or triaxial bulges within primary bars do exist in nature and open new theoretical prospects and challenges by accumulating the problems of non-axisymmetric, time-dependent, non-linear, and dissipative systems.

Acknowledgements. This work has been supported by the Swiss National Science Foundation (FNRS), the French Academy of Sciences, and in part by the NSF through Grant AST 91-16442. We thank the referee, F. Combes, for her valuable comments. DF and HW respectively acknowledge the Steward Observatory and the Geneva Observatory for their kind hospitality.

References

- Athanassoula E., 1983, in: Internal Kinematics and Dynamics of Galaxies, IAU Symp. No. 100, ed. E. Athanassoula. Reidel, Dordrecht, p. 243
- Barth A.J., Ho L.C., Filippenko A.V., Sargent W.L.W., 1995, AJ 110, 1009
- Baumgart C.W., Peterson C.J., 1986, PASP 98, 56
- Benedict G.F., Higdon J.L., Jeffreys W.H., et al., 1993, AJ 105, 1369
- Binney J.J., Gerhard O., 1996, MNRAS (in press)
- Boer B., Schulz H., 1993, A&A 277, 397
- Buta R., 1990, ApJ 351, 62
- Buta R., Crocker D.A., 1993, AJ 105, 1344
- Combes F., 1994, in: Mass-Transfer Induced Activity in Galaxies, ed. I. Shlosman. Cambridge University Press, Cambridge, p. 170
- de Jong R.S., van der Kruit P.C., 1994, A&AS 106, 451
- de Vaucouleurs G., 1974, in: Formation of Galaxies, IAU Symp. No. 58, ed. J.R. Shakeshaft. Reidel, Dordrecht, p. 335
- Elias J.H., Frogel J.A., Matthews K., Neugebauer G., 1982, AJ 87, 1029
- Friedli D., 1996, in: Barred Galaxies, IAU Coll. No 157, eds. R. Buta et al.. ASP Conference Series (in press)
- Friedli D., Benz W., 1995, A&A 301, 649
- Friedli D., Martinet L., 1992, in: Physics of Nearby Galaxies. Nature or Nurture?, eds. T.X. Thuan et al.. Editions Frontières, Gif-sur-Yvette, p. 527
- Friedli D., Martinet L., 1993, A&A 277, 27
- Garcia Gómez C., Athanassoula E., 1991, A&AS 89, 159
- Heller C.H., Shlosman I., 1994, ApJ 424, 84
- Hummel E., van der Hulst J.M., Keel W.C., 1987, A&A 172, 32
- Jarvis B., Dubath P., Martinet L., Bacon R., 1988, A&AS 74, 513
- Knapen J.H., Beckman J.E., Shlosman I., et al., 1995, ApJ 443, L73
- Kormendy J.J., 1979, ApJ 227, 714
- Kormendy J.J., 1982a, ApJ 257, 75
- Kormendy J.J., 1982b, in: Morphology and Dynamics of Galaxies, 12th Advanced Course of the SSAA, eds. L. Martinet, M. Mayor. Geneva Observatory, Geneva, p. 113
- Moorwood A., Finger G., Biereichel P., et al., 1992, The Messenger 69, 61
- Ondrechen M.P., van der Hulst J.M., Hummel E., 1989, ApJ 342, 39
- Pfenniger D., Norman C., 1990, ApJ 363, 391
- Quillen A.C., Frogel J.A., Kuchinski L.E., Terndrup D.M., 1995, AJ 110, 156
- Rhoads J.E., 1996, ApJ (submitted)
- Rix H.-W., Rieke M.J., 1993, ApJ 418, 123
- Saikia D.J., Pedlar A., Unger S.W., Axon D.J., 1994, MNRAS 270, 46
- Sellwood, J., Wilkinson, A., 1993, Rep. Prog. Phys. 56, 173
- Shaw M.A., Combes F., Axon D.J., Wright G.S., 1993, A&A 273, 31
- Shaw M.A., Axon D.J., Probst R., Gatley I., 1995, MNRAS 274, 369
- Shlosman I., Frank J., Begelman M.C., 1989, Nat 338, 45
- Tagger M., Sygnet J.F., Athanassoula E., Pellat R., 1987, ApJ 318, L43
- Terndrup D.M., Davies R.L., Frogel J.A., DePoy D.L., Wells L.A., 1994, ApJ 432, 518
- Telesco C.M., Dressler L.L., Wolstencroft R.D., 1993, ApJ 414, 120
- van Moorsel G.A., 1982, A&A 107, 66
- Wakamatsu K., Nishida M.T., 1980, PASJ 32, 389
- Wozniak H., Friedli D., Martinet L., Martin P., Bratschi P., 1995, A&AS 111, 115 (Paper I)



Fig. 1. For each galaxy in our sample: 1) Greyscale and contour maps in J-band (upper left image), and in K-band (upper right image). Isophotes are spaced by 0.5 mag. except for NGC 1097 whose isophotes are separated by 0.25 mag. 2) Plots of surface brightness μ , ellipticity e and position-angle PA profiles as a function of semi-major axis of the fitted ellipse for JHK-filters from left to right (lower left frame). Each point represents a fitted ellipse. 3) Greyscale of the J-K colour map (lower right image). Black is the bluest, white the reddest. J-H colour map is displayed for NGC 4340 (K-image saturated) and NGC 6782 (K-image not photometric); H-K colour map is shown for NGC 5905 (no J-image). For NGC 1097, only the JHK-images are displayed (photometry not reliable)